

# Multichannel optical atomic magnetometer operating in unshielded environment

Giuseppe Bevilacqua, Valerio Biancalana,\* and Piero Chessa  
*DIISM, University of Siena - Italy*

Yordanka Dancheva  
*DSFTA, University of Siena - Italy*  
(Dated: March 2, 2016)

A multi-channel atomic magnetometer operating in an unshielded environment is described and characterised. The magnetometer is based on  $D_1$  optical pumping and  $D_2$  polarimetry of Cs vapour contained in gas-buffered cells. Several technical implementations are described and discussed in detail. The demonstrated sensitivity of the setup is  $100 \text{ fT}/\sqrt{\text{Hz}}$  when operating in the difference mode.

## I. INTRODUCTION

High sensitivity magnetometers operating in geomagnetic and lower level fields have a wide range of applications in several branches of both fundamental and applied research [1–3]. They are used to both measure and track large scale field variations, such as in geomagnetic surveys [4], and to detect local magnetic variations, such as in measurements of ultra-low-field NMR [5–7] and MRI [8], in relaxometry [9, 10], in biomagnetic applications such as magneto-cardiography [11–14] and in magneto-encephalography [15, 16]. The detection of weak local signals can be performed in small shielded volumes, and indeed this approach is preferable when small sized sources need to be characterised. However, the existence of large sized samples (such as human bodies in biomagnetic measurements), the high costs and the delicateness of shielding devices may prompt the use of alternative methods in order to reject the magnetic noise generated by far-located sources.

Multi-channel sensors [12, 14] open the way for the active compensation of common mode magnetic signals as well as the direct measurement of difference mode signals. Thus, even if top-level sensitivity normally requires operation in shielded volumes, relatively high-sensitivity magnetometry can be profitably performed in open volumes [7, 17] with a more simplified implementation when using sensor operating in non-vanishing fields. Superconducting quantum interference devices (SQUIDS) have traditionally provided the highest magnetometric sensitivity. Recently, the most sensitive atomic magnetometers in the spin-exchange-relaxation-free (SERF) regime, which operate in vanishing fields, have demonstrated their competitiveness with SQUIDS, while also having the advantage of not requiring cryogenic cooling, and of being unaffected by electric noise. Compared to SQUIDS and SERF, other atomic magnetometers have worse sensitivity, although their performance remains better than  $1 \text{ pT}/\sqrt{\text{Hz}}$ , meaning that they are unrivalled by other simpler devices such as Hall and magnetoresistance sen-

sors.

Atomic magnetometry is based on the detection of the Larmor precession of an optically pumped vapour in the field under measurement. The basic working principles of atomic magnetometers date back to over a century ago [18, 19], and the first pioneering implementations date back several decades [20]. Nevertheless, renewed interest in atomic magnetometry has arisen much more recently, thanks to progresses in the knowledge of optical pumping processes [21, 22], and to technical achievements regarding laser sources and atomic sample manufacturing [23]. This set of circumstances has led to important advances in the last decade, so that atomic magnetometers now represent a versatile class of sensors with state-of-the-art sensitivity [2, 24, 25]. In contrast to SQUID magnetometers, which are vector component detectors that measure the field projection along one particular direction, atomic magnetometers (at least in their basic configuration) are scalar in nature, as they measure the modulus of the magnetic field. A scalar sensor operating in a dominant bias field is mainly sensitive to the field variation along the bias field. Thus atomic magnetometers operating in non-vanishing fields are responsive to one component.

Provided that the environmental (bias) field is relatively homogeneous, this kind of magnetometers can be profitably organised into sets of two or more elements to produce a gradiometric response [12, 26], thus rejecting common-mode magnetic noise and identifying signals as weak as several orders of magnitudes below the bias field.

The literature reports several kinds of setups, where various parameters of the pumping radiation are modulated, such as the polarisation [27], the intensity [28] or the optical frequency [26]. A comparison of the different approaches is presented in Ref.[29]. The frequency modulation of the pumping radiation simplifies the implementation (no optical modulators needed), particularly in a dual radiation setup.

In this paper we describe an all-optical atomic magnetometer based on Cs vapour, optically pumped by means of a frequency modulated laser source tuned to the  $D_1$  line, and probed through the rotation of the polarisation plane of a weak linearly polarised beam tuned to the  $D_2$  line. The system contains two composite sensors and the output signals are extracted from two couples of half-

---

\* valerio.biancalana@unisi.it

beam polarimeters, thus obtaining a four-channel system. Depending on the channels selected and on choices at the data analysis stage, this setup enables gradiometric measurements of various orders and with several differently arranged baselines. The sensitivity demonstrated is limited by residual magnetic noise at low frequencies, and, when using the shortest baseline, is essentially determined by the instrumental noise. In this latter configuration the sensitivity level ( $100 \text{ fT}/\sqrt{\text{Hz}}$  in the range  $20 \text{ Hz} \div 100 \text{ Hz}$ ) is comparable to values reported in the literature for similar setups operating in a shielded environment.

## II. SETUP OVERVIEW

### A. Optics

This magnetometer is the evolution of an apparatus described previously [6, 26]. It has two identical arms for differential measurements, but also allows for quadruple channel operation. Each arm (see Fig. 1) contains an illuminator (ILL) providing two co-propagating radiations, a Cs vapour cell, and a dual balanced polarimeter. One of the radiations is resonant with the  $D_1$  transitions of the Cs atoms and is used to optically pump the atoms; the other radiation is near resonant with the  $D_2$  transitions and is used to probe the atomic spins precession. The light generated by the pump laser  $D_1L$  and by the probe laser  $D_2L$  is coupled to a polarisation-maintaining fibre (PMF). A proper mixture of the two lights is accomplished using a  $2 \times 2$  PM on-fibre mixer. Both light sources are based on solid-state continuous-wave lasers. The probe radiation is attenuated by means of an on-fibre attenuator (Att) and is kept at a constant frequency, while the pump radiation is left at the mW level, and is broadly frequency modulated. In the proximity of each vapour cell, the two radiations are collimated into a beam of about 10 mm in diameter, their linear polarisation is reinforced by a polarising cube, and finally a special multi-order waveplate (MOWP) makes the pump radiation circularly polarised, while leaving the probe one linearly polarised.

For this purpose we took advantage of quartz's property of birefringence at the  $D_1$  and  $D_2$  transition wavelengths in Cs. In fact, it is possible [30] to design a multi-order quartz waveplate with a nominal relative delay of 4.75 wavelengths for  $D_1$  radiation and 5.00045 wavelengths for  $D_2$  radiation. Thanks to their low order, the relative delay of such waveplates is only weakly dependent upon misalignment (less than 0.1 % for 1 deg misalignment).

The MOWP technique was similarly employed in another setup described in the literature [15], with several practical advantages that are worthy of mention. In fact, the use of different transitions for the pump and probe processes, facilitates both the alignment (the two radiations are mixed in one fibre, and propagate after collima-

tion along a single optical axis) and the pump suppression after the interaction. This is effectively accomplished by means of an interference filter.

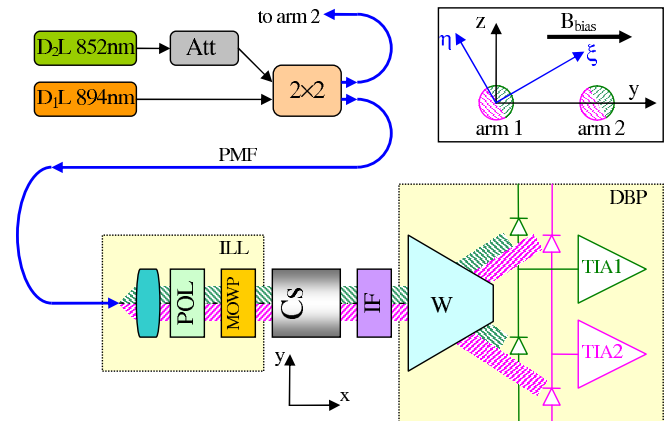


Figure 1. Schematics of a single arm of the magnetometer. The  $D_1L$  pumps the atoms and the  $D_2L$  probes them. The two radiations are mixed in the  $2 \times 2$  coupler, and led to the sensor via a polarisation-maintaining fibre (PMF). At the PMF output, the illuminator (ILL) collimates the two radiations into a single beam and adjusts their polarisation by means of a multi-order wave-plate (MOWP), which renders the polarisation of the pump circular, and leaves the polarisation of the probe linear. The Cs cell is illuminated by the two co-propagating radiations. After interaction with the Cs vapour, the pump radiation is stopped by an interference filter (IF), while the probe impinges on a Wollaston polariser (W) oriented at  $45^\circ$  with respect to the input polarisation plane. A dual balanced polarimeter (DBP) measures the rotation of the probe polarisation plane for the two halves of the beam separately. To this end, the imbalances in the photocurrents flowing in the two couples of series silicon photodiodes are amplified by trans-impedance amplifiers (TIA). The inset represents a front view of the probe beams of both the arms, where the relative orientations of the various baselines and of the bias magnetic field are defined.

### B. Sensor

The atomic sensors are made of high quality sealed cells with flat windows, containing solid source Cs and 23 torr of  $N_2$  as a buffer gas. The vapour density of the Cs is increased by warming the cells up to about  $45^\circ\text{C}$  by means of an alternating current heater. The heater is made of two coaxial coils of thin copper wire wound in an anti-inductive configuration. Possible spurious magnetic fields generated by the heater are rendered of negligible relevance [31] by supplying the coils at 50 kHz, a value largely exceeding the atomic Larmor frequency.

After interaction with the atomic vapour, the pump beam is blocked by an interference filter (IF) [Thorlabs 850/40, with a transmission of 98.5% at 852 nm and an optical density of 4.2 at 894 nm] and the probe beam polarisation is analysed by dual balanced polarimeters

(DBP) made of a  $45^\circ$  oriented Wollaston analyser (W) and two couples of silicon photo-detectors. A similar technique, based on segmented photodetectors, has recently been applied in a higher buffer-gas pressure potassium setup [32]. Each couple of photodetectors measures the polarisation of half a beam (a semicircle in the inset of Fig. 1) by converting the polarisation rotation into a photo-current imbalance, which is in turn amplified and converted into voltage by low-noise trans-impedance amplifiers (TIA). The signal extracted by a balanced polarimeter is proportional to the sinus of twice the polarisation rotation angle. At the maximal observed rotation (about 0.15 rad) the linear approximation results in a 0.35% underestimation, which in the data elaboration is neglected.

The operator may select the channels to be acquired and the corresponding TIA outputs are simultaneously digitised by means of a 16 bit data acquisition card.

The sensors work in a homogeneous magnetic field  $\vec{B}_{\text{bias}}$ , which is obtained by partially compensating the environmental one and is oriented along the  $y$  axis. The longitudinal field component ( $x$ ) is zeroed, and thus the sample magnetisation, which is periodically reinforced along the optical axis, precesses in the  $xz$  plane. Small variations in the field slightly change the resonant precession frequency, or (as discussed in the Appendix) the precession phase when periodic resonant pumping is applied.

### III. PRINCIPLE OF OPERATION

#### A. Laser sources and modulation of the optical frequency

The probe radiation is generated by D<sub>2</sub>L, a single-mode, Fabry-Perot, pigtailed diode laser that is near-resonant with the D<sub>2</sub> line of Cs at 852 nm. This illuminates the cell at a weak intensity, which is attenuated down to a level of a few  $\mu\text{W}/\text{cm}^2$  in order to negligibly perturb the atomic state measured.

The pump radiation is generated by D<sub>1</sub>L, a single-mode, distributed feedback, pigtailed diode laser. Its optical frequency is controlled through the junction current and is periodically made resonant to the transition  $|^2S_{1/2}, F_g = 3\rangle \rightarrow |^2P_{1/2}\rangle$  of Cs at 894 nm. The optical frequency of the pump laser is modulated using a square wave signal generated by a computer-controlled digital-to-analogue converter.

Applying a square wave modulation to the junction current of D<sub>1</sub>L produces a modulation of the optical frequency that cannot easily be described in terms of frequency steps. At least three aspects have to be taken into account in order to evaluate the response to sudden changes in the modulating signal. First of all, the modulation input of the laser driver has a limited bandwidth. This acts as a low-pass filter with a cut-off frequency set at about  $\Gamma_1 = 2\pi \times 25\text{kHz}$  in our case. In addition, when

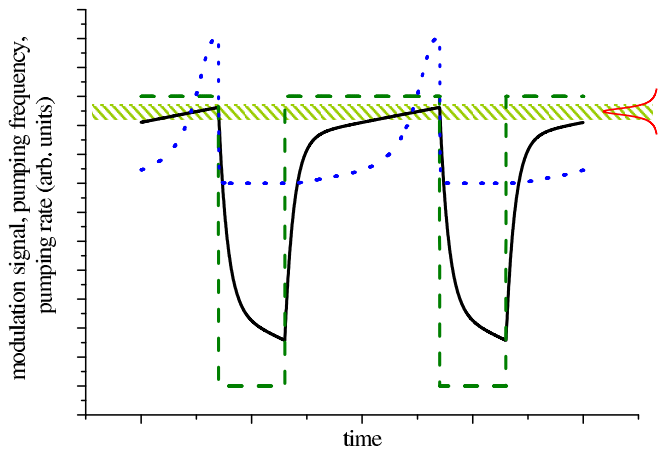


Figure 2. Optical frequency of the D<sub>1</sub>L (solid black) in response to a square wave modulation signal (dashed green). The green hatched band points out the time intervals when D<sub>1</sub>L goes into resonance with an atomic line (rightmost red profile), and the blue dotted line represents the resulting pumping rate. The figure is not to scale, but is produced in accordance with the simple model described by eq. 1. In the text the maximal and minimal frequencies reached in the period will be referred to as *front-* and *back-*frequency, respectively.

changing the junction current, the laser emission changes for two reasons. The first is related to the change of refraction index and has a very quick (instantaneous) response. The second reason is a thermal change of the cavity length, and is a much slower process. The latter introduces a second cut-off frequency at  $\Gamma_2 \approx 2\pi \times 30\text{ Hz}$ . We performed a detailed characterisation, based on techniques involving both atomic and interferometric references [33]). The optical frequency response to a signal at  $\omega$  can be modelled as the sum of two low-pass-filtered terms, and the instantaneous optical frequency deviation can be approximated as

$$\Delta\nu = \sum_{n=0}^{+\infty} \left( \frac{w_1\Gamma_1}{\Gamma_1 + in\omega} + \frac{w_2\Gamma_2}{\Gamma_2 + in\omega_0} \right) V_n + c.c. \quad (1)$$

where  $\Gamma_i$  and  $w_i$  are the cut-off frequencies and weights of the thermal and input filters, respectively, and  $V_n$  are the square wave Fourier components. More precisely, the modulation signal

$$V(t) = \sum_{n=0}^{+\infty} V_n + c.c. = \sum_{n=0}^{+\infty} \frac{2A}{n\pi} \sin(n\pi\delta) e^{ni\omega t} + c.c. \quad (2)$$

is a square wave with amplitude  $A$  and duty cycle  $\delta$ . Typically, the conditions,  $\Gamma_1 \ll \omega$  and  $\Gamma_2 > \omega$  hold. The resulting optical frequency modulation is represented in Fig. 2.

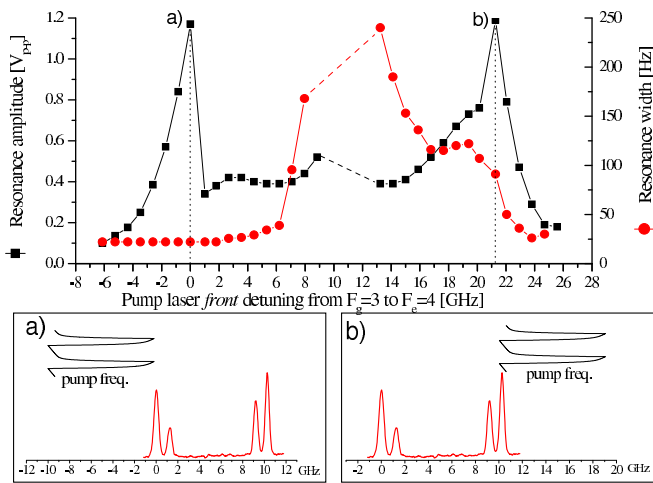


Figure 3. Amplitude and width of the observed resonance line for a fixed D<sub>1</sub>L modulation span, as a function of the front frequency. A square wave modulation signal with a duty cycle of 75% is applied. This produces (see Fig. 2 and eq. 1) the instantaneous D<sub>1</sub>L frequency represented by black lines in the insets, having a span of 11.2 GHz. Two amplitude maxima are observed when either (a) the front frequency is resonant with the leftmost hyperfine component or (b) the back frequency is resonant with the rightmost one. In case (a) the resonance width is minimum, which makes this configuration the optimal working condition. The dashed lines correspond to intermediate detunings, at which no clear resonance line is observed.

### B. Atom-light interaction

The D<sub>1</sub>L optical frequency deviation amounts to tens of GHz, thus the radiation periodically goes in and out of resonance with given transitions of the D<sub>1</sub> line.

Let us define the highest instantaneous optical frequency as *front* frequency and correspondingly the lowest one as *back* frequency (see Figs. 2 and 3). If the frequency deviation is kept constant, when the *front* and the *back* frequencies increase, the amplitude and the width of the magnetic resonance change, as shown in Fig. 3. The probe laser is cw and tuned to be nearly resonant with the triplet  $|^2S_{1/2}, F_g = 4\rangle \rightarrow |^2P_{3/2}\rangle$ , thus it probes the atomic precession of the  $F_g = 4$  state. When the D<sub>1</sub>L approaches the D<sub>1</sub> line from the side of the  $|^2S_{1/2}, F_g = 3\rangle \rightarrow |^2P_{1/2}, F_e = 4\rangle$  transition, the amplitude of the resonance increases, while its width remains almost constant. The amplitude shows two maxima occurring when the *front* frequency goes into resonance with the transitions  $|^2S_{1/2}, F_g = 3\rangle \rightarrow |^2P_{1/2}, F_e = 3, 4\rangle$  (see Fig. 3a)) and when the *back* frequency goes into resonance with the  $|^2S_{1/2}, F_g = 4 \rightarrow |^2P_{1/2}\rangle$  (see Fig. 3b)), respectively.

When D<sub>1</sub>L is near-resonant or resonant with the  $F_g = 4$  (either with its *front* or *back* frequency), the resonance width increases dramatically until the resonance is barely recognisable. In the rightmost region, when the back frequency is near-resonant with the  $F_g = 4$

(Fig. 3b), the resonance amplitude grows again (high-rate Zeeman optical pumping is performed), but the resonance is much broader. Moreover, in this condition a small red detuning results in an abrupt decrease in the signal amplitude, due to hyperfine optical pumping toward the unprobed  $F_g = 3$  ground state.

### C. Sensitivity and optimal working conditions

The modulation duty cycle, amplitude and offset are adjusted to ensure maximum sensitivity. As seen from Fig. 3, the best sensitivity is achieved when the D<sub>1</sub>L *front* frequency is resonant with the  $|^2S_{1/2}, F_g = 3\rangle \rightarrow |^2P_{1/2}\rangle$  hyperfine components of the D<sub>1</sub> line. Concerning the probe laser, its optimal frequency is found to be 2 GHz blue detuned with respect to the triplet  $|^2S_{1/2}, F_g = 4\rangle \rightarrow |^2P_{3/2}\rangle$ , which is an acceptable compromise in order to achieve a good polarisation rotation signal and small excitation rate.

Under these conditions, the pump laser plays two roles: it causes a strong hyperfine optical pumping of the Cs atoms towards the ground state analysed, and simultaneously pumps the atoms into a specific Zeeman sublevel of that state, due to its circular polarisation. The combination of these two effects ensures a high amplitude and small linewidth of the resonance, also thanks to the effect known as light narrowing [34, 35]. The linewidth is also narrow thanks to the fact that the hyperfine ground state measured is weakly perturbed, because D<sub>1</sub>L is either far off-resonance or resonant with the other (depleted) hyperfine ground state.

The Zeeman pumping produces magnetisation of the Cs vapour along the wave-vector ( $x$  direction). As the magnetic field is transverse to the pump light propagation ( $y$  direction), the atomic state where atoms are pumped evolves in time. At a macroscopic scale this corresponds to a magnetisation precession in the  $xz$  plane at an angular frequency  $\omega_L$ , which is set by the magnetic field modulus  $B$  and the gyromagnetic factor  $\gamma$ :  $\omega_L = \gamma B$ . Clearly detectable precessing magnetisation is obtained, again at the macroscopic level, when the pump radiation interacts with the atoms synchronously with the precession.

## IV. OPERATION MODES, FIELD RANGE, RESONANCE LINEWIDTH

The atomic precession is detected by analysing the rotation of the polarisation plane of a weak linearly polarised probe beam, propagating in the  $x$  direction. As is known, the linear polarisation can be regarded as a superposition of two,  $\sigma^+$  and  $\sigma^-$ , counter-rotating circular polarisation components, which experience opposite variations of the refraction index (time dependent circular birefringence). Along the propagation, these two components accumulate different phase delays, and superpose

into a linear polarisation rotated by an angle oscillating at frequency set by the atomic precession. Beside the different dispersions, the  $\sigma^+$  and  $\sigma^-$  components experience also different levels of absorption (circular dichroism), but the relevance of this aspect is limited by appropriately detuning the probe laser from the centre of the atomic resonance.

The polarimetric signal can be analysed as a function of the  $D_1L$  modulation frequency in order to characterise the atomic magnetic resonance, in an operation mode that is referred to as *scanning mode* and enables accurate evaluation of both the precession frequency (used to adjust  $B_{\text{bias}}$ ) and the resonance linewidth observed. The latter is the parameter to be minimised (see below) in the procedure devoted to reducing the field inhomogeneities.

For short-time measurements, it is instead possible to modulate  $D_1L$  with a periodic signal near-resonant with the Larmor precession, and to infer the magnetic field from the dephasing of the polarimetric signal. This operation mode is referred to as *free-running*. It unavoidably suffers from slow drifts of the environmental field, which can eventually lead the system too far from the resonance. This problem is counteracted in a third operation mode (*locked mode*). In this case one of the polarimetric signals is used as an input for a phase-locked loop (PLL) to stabilise the magnetic field [36]. The environmental noise is reduced within the loop bandwidth, and this improves the noise rejection when performing differential measurements, as the spurious common mode noise terms are reduced.

The magnetometer operates in bias magnetic fields ranging from 100 nT to 6  $\mu$ T. Fig. 4 shows the in-phase and quadrature signals of the Cs magnetic resonance as functions of the pump laser modulation frequency, as recorded in the *scanning mode*. The linewidth measured (half-width at half maximum, HWHM) is of the order of 20 Hz and is determined by the spin-exchange collisions and power broadening contributions.

As shown in the Appendix, this linewidth sets the response bandwidth of this kind of sensors, which –with the exception of some specific implementations [37]– corresponds to the cut-off frequency of their response.

The direction of the bias magnetic field is set with the help of three pairs of 1.8 m side square Helmholtz coils (see Refs. [11, 36] for additional details). The magnetic field Jacobian,  $G_{ij} = \partial B_i / \partial x_j$ , is zeroed using five quadrupole devices, taking specific care with the  $\partial B_y / \partial x_i$  elements, which cause static inhomogeneities of  $\delta B_{\parallel}$  and thus most affect the performance. This is coarsely achieved with permanent magnets and then finely adjusted with electromagnets. After such field inhomogeneity compensation, the resonance narrowing is limited –under operative conditions– by the spin-exchange collisions and pump and probe excitation rates. As a matter of fact, when operating at very low Cs densities and excitation rates (at about 10° C), resonances as narrow as 6 Hz are recorded.

In the *free-running* and *locked* modes the field varia-

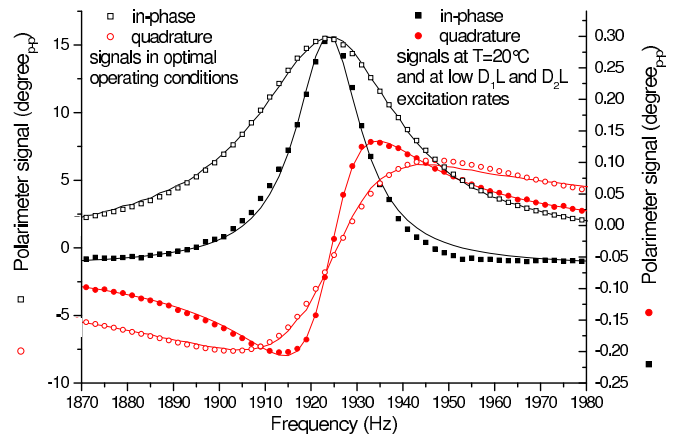


Figure 4. Polarisation rotation of  $D_2L$  radiation (in-phase and quadrature components) as a function of the  $D_1L$  modulation frequency. Dots: values measured, line: best-fit curve, modelled with a Lorentzian profile. The best fit estimation of HWHM is 20 Hz under the optimal working conditions, in which the maximum rotation of  $16^\circ$  peak-to-peak is observed. A narrower line (10 Hz) is obtained at lower temperatures and lower excitation rates, at the expenses of a much smaller rotation ( $0.3^\circ$ ).

tions are inferred from phase estimations of the polarimetric signal. As shown in the Appendix, the phase  $\varphi(t)$  responds to the time-dependent field  $\delta B_{\parallel}(t)$ , according to a first order equation (see eq. (A8)), so that working at the centre of resonance ( $\Delta = 0$ ) its variation is promptly inferred from the measured  $\varphi$  as

$$\delta B_i = \gamma^{-1} [\Gamma \varphi_i + 2f_S (\varphi_{i+1} - \varphi_{i-1})] \quad (3)$$

$f_S$  being the sampling frequency,  $\delta B_i$  the field variation and  $\varphi_i$  the phase, sampled at the times  $t_i$ .

## V. NOISE AND HIGHER-ORDER GRADIOMETRY

As far located (noise) field sources produce mainly common-mode magnetic signals, their contribution can be effectively rejected by performing differential measurements. The principal arms have an adjustable base-line 5.6 cm in the  $y$  direction, with a minimum of 5.6 cm. Each arm is in turn divided in two secondary sections by using segmented photodiodes, as discussed in Sec II B. The array elements are arranged in such a way as to measure the two halves of the laser spot independently, which enables gradiometric measurements with a fixed baseline of 0.5 cm, as well as higher-order gradiometric measurements.

The  $N_2$  buffer gas contained in the sensor cells quenches the fluorescence light avoiding radiation trapping, and slows down the thermal motion of Cs atoms, making it diffusive. The diffusion constant of Cs in  $N_2$  is about  $D=2.4 \text{ cm}^2/\text{s}$  at 23 Torr [38]. Over a time interval as long as the spin relaxation time ( $1/2\pi\Gamma \approx 8 \text{ ms}$ ),

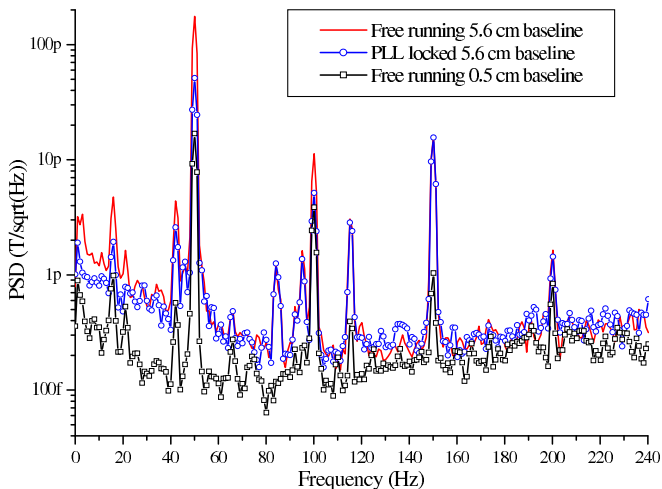


Figure 5. Noise patterns of the difference between two signals obtained in two operation modes. The traces show the RMS values of the power spectral density averaged over 10 measurements. The three spectra correspond to the operation modes reported in the inset.

diffusive displacements of the order of  $\Delta x = 1.4$  mm are thus expected to occur: a distance definitely shorter than the beam radius. The short baseline operation is thus responsive to field inhomogeneities.

If the illuminator and the dual polarimeter (ILL and DBP, respectively, in Fig. 1) of an arm are rigidly mounted, so that they rotate synchronously around the optical axis, gradiometric detection is performed along an arbitrary direction  $\xi$  of the  $yz$  plane (see the inset in Fig. 1) and the system responds with the short baseline to  $\partial B_y / \partial \xi$ . The long baseline is oriented along the  $y$  direction, thus the four channel operation enables measurements of second order terms  $\partial^2 B_y / \partial \xi \partial y$ , which (depending on the alignment) can be varied from  $\partial^2 B_y / \partial y^2$  to  $\partial^2 B_y / \partial y \partial z$ .

Hereafter, let us consider the case in which the three baselines are parallel, i.e. each couple of channels responds proportionally to  $\partial B_y / \partial y$ . When combining the signals from two channels different couples can be chosen, and correspondingly different residual noise is observed. As expected, the bigger the baseline the higher is the residual noise, as shown in Fig. 5.

When applying the PLL field-stabilisation system [36] the noise in the  $y$  direction is actively compensated, which decreases the noise in the frequency range from 0 to 200 Hz, that is the bandwidth of the PLL. The ultimate estimated magnetometer sensitivity, which results from the superposition of detection noise and residual magnetic noise, is of the order of  $100 \text{ fT} / \sqrt{\text{Hz}}$ , as can be seen in Fig. 5 from measurements conducted over a 0.5 cm baseline.

More generally, instead of recording the difference between two signals, it is possible to combine three or four signals in order to achieve optimal noise cancellation. This task is performed by determining the coefficients of

the linear superposition that minimise the variance of the combination in the absence of a signal source. In formula, when acquiring  $N$  channels, the  $N$  signals  $s_k(t)$  with  $k=0, 1, \dots, N-1$  are linearly combined in  $S(t) = \sum_{k=1}^{N-1} a_k s_k(t)$ , where  $a_0$  is set to 1, and  $a_k$  ( $k=1, \dots, N-1$ ) are determined as the ones minimising  $\|S(t)\|^2 = \sum_{i=1}^n S(t_i)^2$ ,  $\{t_i\}$  being the sampling times. Depending on the application, the optimal coefficients  $\{a_k\}$  can be determined after having band-pass-filtered the signals  $s_k(t)$ , in order to achieve the best noise reduction in a specific spectral range.

## VI. CONCLUSION

We have developed and characterised a multichannel optical atomic magnetometer based on a dual arm setup and segmented detectors, enabling polarimetric measurements in transverse subsections of the probe beam, for a total of four independent channels and various alignment-dependent gradiometric arrangements. The setup described makes it possible to perform differential measurements and gradiometric detection over various baselines and different orders. The environmental (common mode) noise-rejection permits the achievement of a noise level as low as a  $100 \text{ fT} / \sqrt{\text{Hz}}$ .

### Appendix A: Polarimetric signal phase

This appendix is devoted to explaining the conditions and the consequent approximations considered in order to infer time-dependent magnetic field variations from the phase of the polarimetric signal.

We refer to the geometry of the experiment reported in Fig. 1 and we assume that the magnetic field is a superposition of two parallel terms: a dominant static term (bias) and a small periodic one

$$\mathbf{B}(t) = (B_{\text{bias}} + \delta B_{\parallel}(t))\hat{y},$$

with  $\delta B_{\parallel}(t + 2\pi/\Omega) = \delta B_{\parallel}(t)$ .

The Larmor equations for the magnetization  $\mathbf{M} = (M_x, M_y, M_z)$  are

$$\begin{aligned} \dot{M}_x &= -\Gamma M_x + (\omega_L + \omega_1(t))M_z + f(t) \\ \dot{M}_y &= -\Gamma M_y \\ \dot{M}_z &= -\Gamma M_z - (\omega_L + \omega_1(t))M_x, \end{aligned}$$

where  $\omega_L = \gamma B_{\text{bias}}$  and  $\omega_1(t) = \gamma \delta B_{\parallel}(t)$  are the Larmor frequencies corresponding to the bias field and to its variation, respectively. In our case  $\omega_L$  is in the kHz range while the damping  $\Gamma_{\parallel}$  and  $\Gamma_{\perp}$  are in the 10 Hz range so we assume they are equal  $\Gamma_{\parallel} = \Gamma_{\perp} = \Gamma$ . The forcing term  $f(t)$  is due to the laser optical pumping and can be calculated exactly, in the approximation of weak laser

power (details will be provided in a forthcoming paper). This term can be expanded in Fourier space as

$$f(t) = \sum_{-\infty}^{+\infty} f_n e^{i\omega t}$$

where  $\omega$  is the laser modulation frequency. The coefficients  $f_n$  satisfy  $f_{-n} = f_n^*$  and for odd  $n$  it can be shown that  $f_n = i|f_n|$ .

Introducing  $M_+ = M_z + iM_y$  the relevant equation of motion becomes

$$\dot{M}_+ = [-\Gamma - i(\omega_L + \omega_1(t))] M_+ + f(t). \quad (\text{A1})$$

The steady-state ( $\Gamma t \gg 1$ ) solution can be written as

$$M_+(t) = e^{-(\Gamma+i\omega_L)t-i\theta_1(t)} \int_0^t e^{+(\Gamma+i\omega_L)t'+i\theta_1(t')} f(t') dt', \quad (\text{A2})$$

where  $\theta_1(t) = \int_0^t \omega_1(t') dt'$ . Introducing the Fourier expansion

$$e^{i\theta_1(t)} = \sum_{-\infty}^{+\infty} G_n e^{in\Omega t} \quad (\text{A3})$$

(in the case that  $B_1(t)$  is sinusoidal the  $G_n$  are the usual Bessel functions) following some algebra we find

$$M_+(t) = \sum_{s,n,m=-\infty}^{+\infty} \frac{G_{n-s}^* G_n f_m}{\Gamma + i\omega_L + im\omega + in\Omega} e^{is\Omega t} e^{im\omega t}. \quad (\text{A4})$$

In the experiment the modulation frequency  $\omega$  is resonant with  $\omega_L$  so that the term with  $m = -1$  is the dominant one. Finally we obtain the expression

$$\begin{aligned} M_+(t) &\approx \sum_{s,n=-\infty}^{+\infty} \frac{G_{n-s}^* G_n f_{-1}}{\Gamma + i(\omega_L - \omega) + in\Omega} e^{is\Omega t} e^{-i\omega t} \\ &\equiv A(t) e^{-i\omega t}, \end{aligned} \quad (\text{A5})$$

which shows, as expected, that the magnetization follows the forcing term with a complex amplitude  $A(t)$ , which has the periodicity of the  $\delta B_{\parallel}(t)$  field.

Although this expression is exact, the double sum hides the interpretation. Moreover, the experiment monitors

the phase of  $M_x(t) = \Re [A(t) e^{-i\omega t}]$  so it is better to work out an equation for  $A(t)$  directly. Assume that the solution  $M_+(t)$  has the form outlined in (A5) and that  $A(t) = a(t) e^{i(\pi/2 + \varphi(t))}$ . The phase  $\varphi(t)$  (the excess of phase from exact resonance) is the quantity monitored in the experiment. Inserting this ansatz in eq.(A1), after some algebra we find

$$\dot{a} = -\Gamma a + |f_{-1}| \cos \varphi \quad (\text{A6a})$$

$$a\dot{\varphi} = -(\Delta + \omega_1)a + |f_{-1}| \sin \varphi, \quad (\text{A6b})$$

where we have introduced the detuning  $\Delta \equiv \omega_L - \omega$  and coherently approximated  $f(t) \approx f_{-1} e^{-i\omega t} = |f_{-1}| e^{i\pi/2} e^{-i\omega t}$ . The laser operates at low power, so the modulus of  $|f_{-1}| \ll \Gamma$  and the  $a(t)$  adiabatically follows

$$a(t) \approx \frac{|f_{-1}|}{\Gamma} \cos \varphi,$$

giving the dynamical equation for the phase

$$\dot{\varphi} = -\Delta - \omega_1(t) - \Gamma \tan \varphi. \quad (\text{A7})$$

This, under our experimental conditions can be linearized as

$$\dot{\varphi} = -\Delta - \omega_1(t) - \Gamma \varphi, \quad (\text{A8})$$

which describes the evolution of the phase as the sum of a damping term ( $-\Gamma\varphi$ ) and a forcing term ( $-\Delta - \omega_1(t)$ ).

The steady-state ( $\Gamma t \gg 1$ ) solution is now elementary

$$\varphi(t) = \frac{\Delta}{\Gamma} + \int_0^t e^{-\Gamma(t-t')} \omega_1(t') dt'. \quad (\text{A9})$$

For a sinusoidal signal  $\omega_1(t) = w \cos(\Omega t + \phi)$  one finds

$$\varphi(t) = \frac{\Delta}{\Gamma} + \frac{w}{\sqrt{\Omega^2 + \Gamma^2}} \cos(\Omega t + \phi - \arctan(\Omega/\Gamma)). \quad (\text{A10})$$

## ACKNOWLEDGMENTS

The authors acknowledge the valuable technical support of Leonardo Stiaccini and the financial support of the Italian Ministry for Research (FIRB project RBAP11ZJFA005). The authors thank Emma Thorley of Language Box (Siena) for revising the English in the manuscript.

---

[1] J. M. Pendlebury, S. Afach, N. J. Ayres, C. A. Baker, G. Ban, G. Bison, K. Bodek, M. Burghoff, P. Geltenbort, K. Green, W. C. Griffith, M. van der Grinten, Z. D. Grujić, P. G. Harris, V. Hélaine, P. Iaydjiev, S. N. Ivanov, M. Kasprzak, Y. Kermaidic, K. Kirch, H.-C. Koch, S. Komposch, A. Kozela, J. Krempel, B. Lauss, T. Lefort, Y. Lemière, D. J. R. May, M. Musgrave, O. Naviliat-

Cuncic, F. M. Piegsa, G. Pignol, P. N. Prashanth, G. Quémener, M. Rawlik, D. Rebreyend, J. D. Richardson, D. Ries, S. Rocca, D. Rozpedzik, A. Schnabel, P. Schmidt-Wellenburg, N. Severijns, D. Shiers, J. A. Thorne, A. Weis, O. J. Winston, E. Wursten, J. Zejma, and G. Zsigmond, "Revised experimental upper limit on the electric dipole moment of the neutron," *Phys. Rev.*

- D*, vol. 92, p. 092003, Nov 2015.
- [2] D. Budker and M. Romalis, "Optical magnetometry," *Nature Physics*, vol. 3, pp. 227–234, 2007.
  - [3] A. Wickenbrock, S. Jurgilas, A. Dow, L. Marmugi, and F. Renzoni, "Magnetic induction tomography using an all-optical 87rb atomic magnetometer," *Opt. Lett.*, vol. 39, pp. 6367–6370, Nov 2014.
  - [4] L. Lenci, S. Barreiro, P. Valente, H. Failache, and A. Lezama, "A magnetometer suitable for measurement of the earth's field based on transient atomic response," *Journal of Physics B: Atomic, Molecular and Optical Physics*, vol. 45, no. 21, p. 215401, 2012.
  - [5] I. M. Savukov and M. V. Romalis, "NMR Detection with an Atomic Magnetometer," *Physical Review Letters*, vol. 94, p. 123001, Mar. 2005.
  - [6] G. Bevilacqua, V. Biancalana, Y. Dancheva, and L. Moi, "Chapter three - optical atomic magnetometry for ultra-low-field nmr detection," vol. 78 of *Annual Reports on NMR Spectroscopy*, ch. 3, pp. 103 – 148, Academic Press, 2013.
  - [7] G. Bevilacqua, V. Biancalana, A. B.-A. Baranga, Y. Dancheva, and C. Rossi, "Microtesla nmr j-coupling spectroscopy with an unshielded atomic magnetometer," *Journal of Magnetic Resonance*, vol. 263, pp. 65 – 70, 2016.
  - [8] I. Savukov and T. Karaulanov, "Anatomical {MRI} with an atomic magnetometer," *Journal of Magnetic Resonance*, vol. 231, pp. 39 – 45, 2013.
  - [9] P. J. Ganssle, H. D. Shin, S. J. Seltzer, V. S. Bajaj, M. P. Ledbetter, D. Budker, S. Knappe, J. Kitching, and A. Pines, "Ultra-low-field nmr relaxation and diffusion measurements using an optical magnetometer," *Angewandte Chemie International Edition*, vol. 53, no. 37, pp. 9766–9770, 2014.
  - [10] V. Dolgovskiy, V. Lebedev, S. Colombo, A. Weis, B. Michen, L. Ackermann-Hirschi, and A. Petri-Fink, "A quantitative study of particle size effects in the magnetorelaxometry of magnetic nanoparticles using atomic magnetometry," *Journal of Magnetism and Magnetic Materials*, vol. 379, pp. 137 – 150, 2015.
  - [11] J. Belfi, G. Bevilacqua, V. Biancalana, S. Cartaleva, Y. Dancheva, and L. Moi, "Cesium coherent population trapping magnetometer for cardiosignal detection in an unshielded environment," *JOSA B*, vol. 24, no. 9, pp. 2357–2362, 2007.
  - [12] G. Bison, N. Castagna, A. Hofer, P. Knowles, J.-L. Schenker, M. Kasprzak, H. Saudan, and A. Weis, "A room temperature 19-channel magnetic field mapping device for cardiac signals," *Applied Physics Letters*, vol. 95, no. 17, pp. –, 2009.
  - [13] K. Kamada, Y. Ito, and T. Kobayashi, "Human mcg measurements with a high-sensitivity potassium atomic magnetometer," *Physiological Measurement*, vol. 33, no. 6, p. 1063, 2012.
  - [14] O. Alem, T. H. Sander, R. Mhaskar, J. LeBlanc, H. Eswaran, U. Steinhoff, Y. Okada, J. Kitching, L. Trahms, and S. Knappe, "Fetal magnetocardiography measurements with an array of microfabricated optically pumped magnetometers," *Physics in Medicine and Biology*, vol. 60, no. 12, p. 4797, 2015.
  - [15] C. Johnson, P. D. D. Schwindt, and M. Weisend, "Magnetoencephalography with a two-color pump-probe, fiber-coupled atomic magnetometer," *Applied Physics Letters*, vol. 97, no. 24, pp. –, 2010.
  - [16] H. Xia, A. Ben-Amar Baranga, D. Hoffman, and M. V. Romalis, "Magnetoencephalography with an atomic magnetometer," *Applied Physics Letters*, vol. 89, no. 21, pp. –, 2006.
  - [17] G. Bevilacqua, V. Biancalana, Y. Dancheva, and L. Moi, "All-optical magnetometry for NMR detection in a micro-Tesla field and unshielded environment," *Journal of Magnetic Resonance*, vol. 201, pp. 222–229, Dec. 2009.
  - [18] D. Macaluso and O. M. Corbino, "Sopra Una Nuova Azione Che La Luce Subisce Attraversando Alcuni Vapori Metallici In Un Campo Magnetico," *Nuovo Cimento*, vol. 8, p. 257, 1898.
  - [19] D. Macaluso and O. M. Corbino, "Sulla Relazione Tra Il Fenomeno Di Zeemann E La Rotazione Magnetica Anomala Del Piano Di Polarizzazione Della Luce," *Nuovo Cimento*, vol. 9, p. 384, 1899.
  - [20] W. E. Bell and A. L. Bloom, "Optically driven spin precession," *Phys. Rev. Lett.*, vol. 6, pp. 280–281, Mar 1961.
  - [21] W. Happer, "Optical pumping," *Rev. Mod. Phys.*, vol. 44, pp. 169–249, Apr 1972.
  - [22] M. Auzinsh, D. Budker, and S. Rochester, *Optically Polarized Atoms: Understanding Light-atom Interactions*. OUP Oxford, 2010.
  - [23] V. Shah, S. Knappe, P. D. D. Schwindt, and J. Kitching, "Subpicotesla atomic magnetometry with a microfabricated vapour cell," *Nature Photonics*, vol. 1, pp. 649–652, Nov. 2007.
  - [24] W. Chalupczak, R. M. Godun, S. Pustelny, and W. Gawlik, "Room temperature femtotesla radio-frequency atomic magnetometer," *Applied Physics Letters*, vol. 100, p. 242401, June 2012.
  - [25] D. Sheng, S. Li, N. Dural, and M. V. Romalis, "Sub-femtotesla scalar atomic magnetometry using multipass cells," *Phys. Rev. Lett.*, vol. 110, p. 160802, Apr 2013.
  - [26] J. Belfi, G. Bevilacqua, V. Biancalana, S. Cartaleva, Y. Dancheva, K. Khanbekyan, and L. Moi, "Dual channel self-oscillating optical magnetometer," *JOSA B*, vol. 26, no. 5, pp. 910–916, 2009.
  - [27] E. Breschi, Z. D. Grujić, P. Knowles, and A. Weis, "A high-sensitivity push-pull magnetometer," *Applied Physics Letters*, vol. 104, no. 2, 2014.
  - [28] Z. Jun-Hai, L. Qiang, Z. Xian-Jin, L. Jiu-Xing, and S. Wei-Min, "All-optical cesium atomic magnetometer with high sensitivity," *Chinese Physics Letters*, vol. 29, no. 6, p. 068501, 2012.
  - [29] Z. D. Grujić and A. Weis, "Atomic magnetic resonance induced by amplitude-, frequency-, or polarization-modulated light," *Phys. Rev. A*, vol. 88, p. 012508, Jul 2013.
  - [30] L. L. C. Optisource, "Multi-order waveplate specification," *private communication*, 2010.
  - [31] G. Bevilacqua, V. Biancalana, Y. Dancheva, and L. Moi, "Larmor frequency dressing by a nonharmonic transverse magnetic field," *Phys. Rev. A*, vol. 85, p. 042510, Apr. 2012.
  - [32] D. A. Keder, D. W. Prescott, A. W. Conovaloff, and K. L. Sauer, "An unshielded radio-frequency atomic magnetometer with sub-femtotesla sensitivity," *AIP Advances*, vol. 4, no. 12, pp. –, 2014.
  - [33] Y. Dancheva, V. Biancalana, D. Pagano, and F. Scortecchi, "Measurement of XeI and XeII velocity in the near exit plane of a low-power Hall effect thruster by light induced fluorescence spectroscopy," *Review of Scientific Instruments*, vol. 84, p. 065113, June 2013.

- [34] S. Appelt, A. Ben-Amar Baranga, A. R. Young, and W. Happer, "Light narrowing of rubidium magnetic-resonance lines in high-pressure optical-pumping cells," *Phys. Rev. A*, vol. 59, pp. 2078–2084, Mar 1999.
- [35] T. Scholtes, V. Schultze, R. IJsselsteijn, S. Woetzel, and H.-G. Meyer, "Light-narrowed optically pumped  $M_x$  magnetometer with a miniaturized cs cell," *Phys. Rev. A*, vol. 84, p. 043416, Oct 2011.
- [36] J. Belfi, G. Bevilacqua, V. Biancalana, R. Cecchi, Y. Dancheva, and L. Moi, "Stray magnetic field compensation with a scalar atomic magnetometer," *Review of Scientific Instruments*, vol. 81, no. 6, p. 065103, 2010.
- [37] A. Terao, K. Ban, S. Ichihara, N. Mizutani, and T. Kobayashi, "Highly responsive ac scalar atomic magnetometer with long relaxation time," *Phys. Rev. A*, vol. 88, p. 063413, Dec 2013.
- [38] N. Beverini, P. Minguzzi, and F. Strumia, "Foreign-Gas-Induced Cesium Hyperfine Relaxation," *Phys. Rev. A*, vol. 4, pp. 550–555, Aug. 1971.